J Adv Ceram

Research Article

Joule heating-driven ultrafast synthesis of $(Fe_{1-x}Mn_x)_2AlB_2$ and its electromagnetic wave absorption properties

Yuhang Bai[1,2], Zelong Yao[1], Yang Yang[1], Jinrui Li[1], Jia Liu[1], Peipei Wang[1], Huiling Du[1], Xing Zhao[1,✉], Laifei Cheng[2,✉]

Cite this article: Bai Y, Yao Z, Yang Y, et al. *J Adv Ceram* 2025, **14**(4): 9221057. https://doi.org/10.26599/JAC.2025.9221057

ABSTRACT: Defect engineering enables the efficient management of electromagnetic parameters and the enhancement of electromagnetic wave (EMW) absorption. In this study, $(Fe_{1-x}Mn_x)_2AlB_2$ transition metal boride (MAB) phases with a layered structure were prepared via Joule heating-driven ultrafast synthesis, and their EMW absorption properties were investigated. The experimental results demonstrate that the incorporation of Mn atoms at the M site can effectively modulate the impedance matching and EMW absorption properties of the material through the introduction of defects and lattice distortions. Notably, $(Fe_{0.3}Mn_{0.7})_2AlB_2$ exhibits a reflection loss as high as −47.8 dB at 12.24 GHz, with a maximum effective absorption bandwidth of 4.16 GHz (10.24–14.40 GHz) at an ultrasmall thickness of 1.5 mm. This study provides a promising avenue for the development of excellent microwave-absorbing materials, which are essential for meeting the evolving requirements of advanced electronics. Additionally, this work offers a paradigm for enhancing other properties of MAB phases through defect engineering.

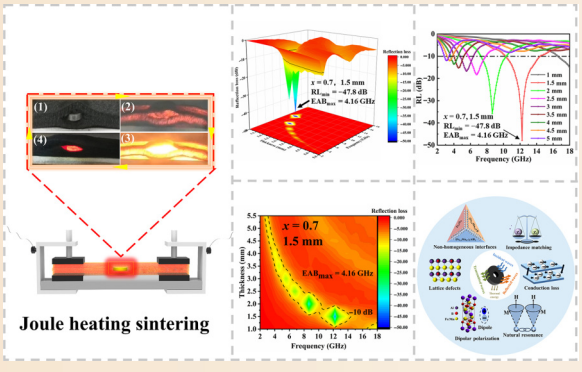

KEYWORDS: electromagnetic wave absorption; defect engineering; Joule heating-driven ultrafast synthesis; transition metal boride phases

1 Introduction

The ubiquitous exposure to electromagnetic waves (EMWs) resulting from the proliferation of electronic devices poses significant implications for human health [1–3]. Consequently, there is an increasing demand for EMW-absorbing materials that exhibit broadband performance, strong EMW absorption, and lightweight properties to address this issue and perform multiple functionalities [4]. Transition metal boride (MAB) phases, which comprise a transition metal element (M), a group-A element (IIIA or IVA), and boron (B), exhibit good physicochemical properties, such as high electrical and thermal conductivity, as well as nano-lamellar microstructure [5]. The combination of these attributes makes MAB phases exceptionally promising candidates for microwave absorption applications [6].

Fe_2AlB_2, a typical MAB phase, exhibits considerable potential as an effective wave-absorbing material because of its low density (5.57 g/cm^3), metal-like electrical conductivity, ferromagnetic properties, and magnetothermal effect [7–10]. However, its magnetic loss capacity is relatively limited, which limits its wave absorption ability. To address this, the deliberate incorporation of magnetic elements (such as Fe, Co, Ni, and Mn) through doping has been proposed as a strategy to maintain the excellent dielectric properties of the material while simultaneously enhancing its magnetic loss, thereby improving its overall ability to absorb EMW—a concept that has been successfully applied to various materials. For instance, Luo *et al.* [11] increased the charge density around the M-site atoms of Ti_2AlC by introducing defects through V and Cr doping. This variation in the charge density favors the formation of dipoles, with the dipole strength increasing with increasing amounts of V or Cr added, thus enhancing the polarization loss of the material. The sample prepared via this approach had a minimum reflection loss (RL_{min}) of −56.2 dB and good EMW absorption properties. Similarly, Li *et al.* [12] doped the M site of Ti_3AlC_2 with Fe, which resulted in a significantly enhanced magnetic loss due to the introduction of both magnetic components and defects. The layered Ti_3AlC_2 structure and coexisting phases expand the active interface, enhancing the local polarization and improving the microwave absorption capabilities of the material. Owing to the combined effects of dielectric and magnetic losses, the resulting Fe-doped Ti_3AlC_2 possessed an RL_{min} of −33.3 dB. Using a similar strategy, Han *et al.* [13]

[1] School of Material Science and Engineering, Xi'an University of Science and Technology, Xi'an 710054, China. [2] Science and Technology on Thermostructural Composite Materials Laboratory, Northwestern Polytechnical University, Xi'an 710072, China.

✉ Corresponding authors. E-mail: X. Zhao, zhaoxing@xust.edu.cn; L. Cheng, chenglf@nwpu.edu.cn

Received: January 6, 2025; Revised: February 25, 2025; Accepted: February 26, 2025

introduced defects by doping the M site of V_2AlC with magnetic elements (Fe, Co, Ni, and Mn). The addition of these magnetic elements expanded the non-uniform interface between the high-entropy MAX phase (X is carbon or nitrogen) and paraffin wax, enhancing the interfacial polarization. The natural resonance and eddy current losses due to the incorporation of magnetic elements endowed the material with effective magnetic losses and improved impedance matching, resulting in RL_{min} of −37.4 dB. Given the structural similarities between the MAX and MAB phases, it is believed that the same doping approaches can be applied to MAB phases. Thus, optimizing the magnetic loss capability of Fe_2AlB_2 through M-site doping with magnetic elements has become a research hotspot for enhancing its wave-absorption performance.

The incorporation of Mn at the M site appears to be an effective way to enhance the magnetic loss of Fe_2AlB_2. Mn_2AlB_2 shows antiferromagnetic ordering below a Néel temperature (T_N) of 313 K [14]. The antiferromagnetic properties of Mn_2AlB_2 allow it to interact with Fe_2AlB_2, which displays ferromagnetic characteristics. This interaction results in a magnetization jump, which is typically accompanied by a significant change in the saturation magnetization [14]. Melikhov *et al.* [15] studied the effects of Mn doping and adjustment of the Fe–Mn atomic ratio on the magnetic anisotropy of $CoMn_xFe_{2-x}O_4$ ferrites and concluded that Mn doping reduced the magnetic anisotropy of ferrite crystals. The reduction in the magnetic anisotropy of these crystals leads to a shift in their natural resonance frequency, which in turn causes an increase in natural resonance loss upon approaching the working frequency [16]. Furthermore, Shiotani *et al.* [14] developed $(Fe_{1-x}Mn_x)_2AlB_2$ with coexisting ferromagnetic and antiferromagnetic states through Mn doping, and they reported that the direction of the magnetic moment of this system changed upon increasing Mn concentration. This change induces natural resonance loss when the direction of the magnetic moment aligns with the applied magnetic field as the magnetic domains gradually rotate. Therefore, incorporating Mn at the M site is an effective way to enhance the magnetic loss of Fe_2AlB_2. Additionally, the ability to precisely adjust the Fe–Mn atomic ratio is a significant challenge that needs to be addressed.

Currently, MAB phases are typically prepared via powder solid-phase reaction sintering at high temperatures in muffle or tube furnaces. This method presents several disadvantages, including a slow temperature rise, volatilization of material elements, and inhomogeneous composition (due to segregation) of obtained materials [17]. A low heating rate leads to an increased grain size, which reduces the number of interfaces and defects within the material [18]. These interfaces and defects are crucial for EMW scattering and absorption [19]. Therefore, developing a rapid heating methodology that can be used to prepare MAB phases with suitable wave-absorption performance is urgently needed. Joule heating-driven ultrafast synthesis is notable for its high heating (10^3–10^4 °C/min) and cooling (10^4 °C/min) rates, as well as its ability to reach ultrahigh temperatures, up to 3000 °C. This high heating rate allows samples to quickly pass through the temperature range where only grain coarsening occurs, promoting grain refinement and consequently introducing more interfaces and defects. This method has also been shown to be effective for synthesizing a wide range of materials, such as $BaTiO_3$ and lead zirconate titanate (PZT) [20–22]. Therefore, it is reasonable to believe that this rapid preparation method can effectively shorten the sintering time, reduce element volatilization and unnecessary interdiffusion, and facilitate the precise tuning of the Fe–Mn atomic ratio.

In this study, $(Fe_{1-x}Mn_x)_2AlB_2$ samples (x = 0, 0.2, 0.4, 0.5, 0.7, and 1) were successfully prepared via Joule heating-driven ultrafast synthesis within 12 s at approximately 930 °C. The EMW absorption properties of the prepared materials and the associated dielectric and magnetic loss mechanisms were investigated. Mn doping introduces non-homogeneous interfaces and defects in Fe_2AlB_2, which results in high interfacial and dipole polarizations. Additionally, by optimizing the impedance matching through the synergistic effects of dielectric and magnetic losses, the EMW absorption capability of the material is enhanced. Notably, $(Fe_{0.3}Mn_{0.7})_2AlB_2$ exhibits a reflection loss as high as −47.8 dB at 12.24 GHz with a maximum effective absorption bandwidth (EAB_{max}) of 4.16 GHz (10.24–14.40 GHz) at an ultrasmall thickness of 1.5 mm. This achievement can be attributed to the change in the magnetic moment and the occurrence of a super-magnetic jump at approximately x = 0.7, which enhances the saturation magnetization and magnetic loss of the material [14]. The present work demonstrates the significant potential of doping MAB phases with magnetic elements to modulate their dielectric and magnetic losses and thus enhance their wave-absorption properties. Furthermore, this study provides a valuable reference for exploring the potential applications of other MAB phases as EMW absorbers.

2 Experimental materials and methods

2.1 Materials

High-purity commercial powders of Fe (99 wt%, 10 μm), B (99 wt%, 10–20 μm), Mn (99 wt%, 10 μm), and Al (99 wt%, 1 μm), as well as anhydrous ethanol, were obtained from Beijing InnoChem Science & Technology Co., Ltd., China). Carbon felt was purchased from Jiangxi Shuobang New Materials Technology Co., Ltd., China).

2.2 Synthesis of $(Fe_{1-x}Mn_x)_2AlB_2$ powders

To prepare the $(Fe_{1-x}Mn_x)_2AlB_2$ samples, suitable quantities of Fe, Mn, Al, and B powders were blended according to stoichiometric ratios, that is, $(Fe_{1-x}Mn_x)$: Al : B = 2 : 1 : 2 (where x = 0, 0.2, 0.4, 0.5, 0.7, and 1). Additionally, 10 wt% excess Al was incorporated into the mixture to compensate for potential Al volatilization. The mixtures were then subjected to wet ball milling using polytetrafluoroethylene (PTFE) jars, onyx balls, and ethanol as the grinding media. The wet ball milling process was conducted at 300 r/min for 12 h. Following milling, the material was dried in an oven at 60 °C for 10 h. Subsequently, 0.3 g of the dried powder was pressed into a cylindrical bulk with dimensions of ϕ10 mm × 3 mm under a pressure of 30 MPa. The pressed billet was positioned centrally within a carbon felt, which measured 110 mm in length, 22 mm in width, and 5 mm in thickness. Afterwards, the carbon felt was affixed between the two end electrodes using a clamp. The electrodes were placed in a vacuum chamber and connected to a programmable direct current (DC) power supply (PS91000-30, Elektro-Automatik, Germany) outside the chamber via a vacuum electrode. The vacuum chamber was sealed, and a mechanical pump was used to evacuate the chamber until the pressure dropped below 200 Pa. Sintering was carried out using a home-made Joule heating-driven ultrafast synthesis device (as shown in Fig. 1) [23,24], which was heated to ~930 °C under vacuum conditions at a heating rate of 10^3–10^4 °C/min. The sintering curves and sintering parameters of $(Fe_{1-x}Mn_x)_2AlB_2$ powders are presented in Fig. S1 and Table S1 in the Electronic Supplementary Material (ESM), respectively. Following sintering, the power was turned off, and the material was allowed to cool naturally to room temperature; the complete sintered blocks were

taken out of the chamber and pulverized into powder for further analysis and utilization. The details of the preparation process of $(Fe_{1-x}Mn_x)_2AlB_2$ powders are illustrated in the flowchart in Fig. 1.

2.3 Characterizations

Phase structure analysis was carried out using an X-ray diffractometer (XRD; AXS D8 Advance, Bruker, Germany) equipped with a Cu Kα radiation source, and crystal structure analysis was performed via Rietveld refinement using the GSAS Rietveld software. The microstructure of $(Fe_{1-x}Mn_x)_2AlB_2$ samples was investigated using a field-emission scanning electron microscope (SEM; QUANTA 250 FEG, FEI, USA) and a transmission electron microscope (TEM; 1400Flash, JEOL, Japan) in conjunction with energy-dispersive X-ray spectroscopy (EDX). The chemical state of the samples was investigated via an X-ray photoelectron spectrometer (XPS; Axis Ultra DLD, Kratos, UK). To investigate the magnetic properties of $(Fe_{1-x}Mn_x)_2AlB_2$ samples, room-temperature hysteresis loops were recorded to determine the saturation magnetization. A vibrating sample magnetometer (PPMS-VSM; 7404, LakeShore, USA) was used for these measurements.

2.4 EMW absorption measurements

To evaluate the EMW absorption performance of the samples, each sample was mixed with paraffin at a mass ratio of 6 : 4. Subsequently, the mixture was pressed into a ring with an outer diameter of 7.0 mm, an inner diameter of 3.0 mm, and a thickness of 2.0–2.3 mm. The electromagnetic (EM) parameters of the prepared samples were measured using a vector network analyzer (VNA; AV3656D, Ceyear, China) in the frequency range of 2–18 GHz, employing the coaxial method.

3 Results and discussion

3.1 Characterizations of phase composition and microstructure

Figure 1 illustrates the details of the preparation process of $(Fe_{1-x}Mn_x)_2AlB_2$ powders. The Joule heating process comprises four distinct stages. (1) Pre-sintering stage: The color of the carbon felt and the sample is the same. (2) Initial rapid heating stage: The carbon felt and the sample gradually turn red. (3) Intermediate stage with a slight temperature increase: The color of the carbon felt and the sample transitions from red to golden yellow. (4) Cooling stage: The carbon felt returns to its original black color, while the sample remains red. The red hue gradually dissipates as the sample cools to room temperature. The Joule heating-driven ultrafast synthesis method can achieve heating and cooling rates of up to 10^4 °C/min, which markedly enhances the efficiency of the preparation process in comparison to the conventional sintering method based on resistance heating (where the heating rate is typically less than 50 °C/min and the cooling rate is approximately 5 °C/min).

Figure 2(a) presents the XRD patterns of $(Fe_{1-x}Mn_x)_2AlB_2$ samples with x = 0, 0.2, 0.4, 0.5, 0.7, and 1. Notably, the diffraction peaks of the parent phases in the x = 0 and x = 1 samples align precisely with the reference patterns PDF#04-007-5354 (Fe_2AlB_2) and PDF#97-002-5518 (Mn_2AlB_2), respectively. For Mn-doped samples (x = 0.2–0.7), the primary diffraction peaks progressively shift between the characteristic peaks of Fe_2AlB_2 and Mn_2AlB_2. The observed intermediate diffraction peak position can be attributed to the difference in the atomic radius between Mn and Fe, which induces systematic variations in the lattice parameters. Minor by-products are detected in all synthesized samples. Specifically, the XRD pattern of the pristine Fe_2AlB_2 (x = 0) reveals distinct peaks at 2θ = 22.43°, 26.66°, 43.01°, and 44.18°, corresponding to the (003), (022), (332), and (025) planes of the intermetallic compound Fe_4Al_{13}. The presence of Fe_4Al_{13} can be attributed to the partial decomposition of Fe_2AlB_2, facilitated by enhanced Al–Fe interactions under high-temperature synthesis conditions [25]. Similar Fe_4Al_{13} signatures persist in samples with x = 0.2–0.7. Additionally, Mn doping introduces additional peaks at 2θ = 37.42°, 40.93°, and 47.20°, which are indexed the (011), (111), and (102) planes of $(Fe_{0.4}Mn_{0.6})B$ phase. These features confirm the partial incorporation of Mn into the Fe sublattice during synthesis [26]. For the sample with x = 1, the diffraction peaks observed at 2θ = 26.80°, 37.15°, 38.97°, 40.60°, 44.55°, and 46.73° correspond to the (101), (011), (201), (111), (210), and (102) crystallographic planes of MnB phase, respectively. Consequently, the previously identified $(Fe_{0.4}Mn_{0.6})B$ phase disappears, while MnB emerges as the dominant secondary phase [26]. Notably, the formation of boride- and intermetallic-based secondary phases is thermodynamically inevitable during the synthesis of MAB phases [25]. Intriguingly, these by-products contribute additional heterogeneous interfaces, thereby enhancing the EMW absorption performance of the material [27]. To characterize the crystal structure parameters of $(Fe_{1-x}Mn_x)_2AlB_2$ samples quantitatively, Rietveld refinement of the XRD patterns was performed using the GSAS software. As shown in Fig. S2 and Table S2 in the ESM, the refinement parameters yield reliability factors (R_p and R_{wp}) ranging from 2.89%–6.30% and 3.65%–9.80%, respectively. Collectively, these results validate the efficacy of ultrafast Joule heating-driven synthesis method in the production of $(Fe_{1-x}Mn_x)_2AlB_2$ materials.

The surface electronic states of $(Fe_{1-x}Mn_x)_2AlB_2$ were systematically investigated using XPS. As clearly shown in Fig. 2(b), the XPS survey spectrum of pristine Fe_2AlB_2 (x = 0) confirms the coexistence of five elements: Fe, O, C, B, and Al. Progressive Mn substitution induces notable spectral evolution. At x = 0.7, characteristic Mn 2p peaks emerge while residual Fe 2p signals

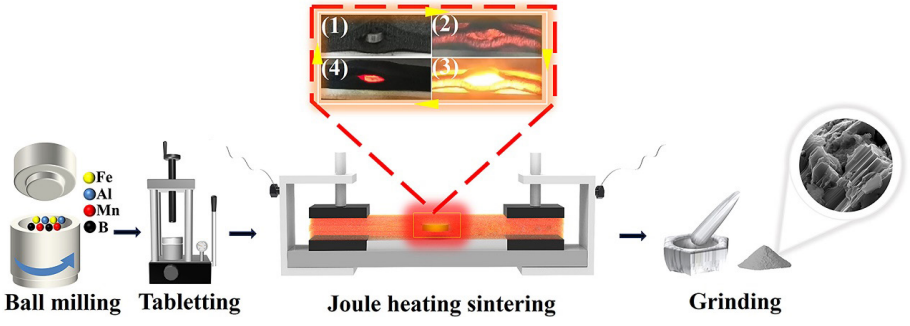

Fig. 1 Diagram illustrating preparation process of $(Fe_{1-x}Mn_x)_2AlB_2$ powders.

persist alongside other constituent elements. Full substitution (x = 1, Mn_2AlB_2) results in the complete disappearance of Fe 2p features, yielding a spectrum dominated exclusively by Mn, O, C, B, and Al components. This systematic evolution provides direct evidence for the full compositional transition from Fe- to Mn-based MAB phases through substitutional doping. To further elucidate the chemical states, Figs. 2(c)–2(f) present the high-resolution XPS spectra of Fe 2p, Mn 2p, Al 2p, and B 1s for the representative $(Fe_{0.3}Mn_{0.7})_2AlB_2$ sample. The Fe 2p spectrum exhibits characteristic peaks at 706.41 and 719.1 eV, corresponding to Fe $2p_{3/2}$ and Fe $2p_{1/2}$, respectively. The Mn 2p spectrum displays complexity with three distinct oxidation states: The primary peaks at 640.8 and 652.1 eV are assigned to Mn^{2+} $2p_{3/2}$ and Mn^{2+} $2p_{1/2}$, respectively, whereas those at 642.3/652.9 and 643.2/654.2 eV are attributed to Mn^{3+} and Mn^{4+} species, respectively. The observed coexistence of Mn^{2+}, Mn^{3+}, and Mn^{4+} oxidation states likely originates from minor surface oxidation [27–29]. Additionally, the Al 2p (74.10 eV) and B 1s (187.95 eV) binding energies align well with reported values for MAB phase compounds. Combined with the comparative XPS data for Fe_2AlB_2 and Mn_2AlB_2 (Figs. S3 and S4 in the ESM), these results validate the successful synthesis of $(Fe_{1-x}Mn_x)_2AlB_2$ solid solutions across the entire composition range.

Figures 3(a) and 3(b) show SEM images of $(Fe_{0.3}Mn_{0.7})_2AlB_2$ sample, which reveal a clear laminar structure and presence of grains. The particle size distribution of $(Fe_{0.3}Mn_{0.7})_2AlB_2$ sample shown in Fig. S5 in the ESM is approximately normal, with an average particle size (D_{50}) of 9.537 μm and D_{90} (D_{90} is defined such that 90% of the particles have a diameter smaller than or equal to this value) of 23.328 μm. For comparison, the average particle size of Fe_2AlB_2 prepared using the combustion synthesis hot-pressing method in a previous work was reported to be 12.8 μm, with a maximum particle size of 57 μm [30]. This result confirms that the grain size can be effectively refined through Joule heating-driven ultrafast synthesis. Within MAB phase systems, reduced particle dimensions yield increased specific surface areas that amplify EMW–material interactions via multiscale scattering phenomena and energy dissipation mechanisms. Crucially, the reduced-dimensional particles intensify interfacial polarization effects, enabling efficient electromagnetic energy conversion through thermal dissipation processes. Figure 3(c) presents the high-angle annular dark-field scanning transmission electron microscopy (HAADF-STEM) images and corresponding EDS elemental mapping images, which show a uniform distribution of Fe, Mn, Al, and B elements. Figure 3(d) shows a high-resolution transmission electron microscopy (HRTEM) image, which clearly displays lattice fringes with a spacing of 0.229 nm (calculated by averaging the total distance across 20 planes), which corresponds to the (130) crystal planes of $(Fe_{0.3}Mn_{0.7})_2AlB_2$. Figure 3(e) exhibits discontinuous lattice fringes, indicating the presence of lattice deficiencies within the grains. These structural defects are attributed primarily to the ultrafast Joule-heating process, which kinetically suppresses surface diffusion-mediated defect healing. The truncated thermal exposure (< 12 s dwell time) prevents the atomic rearrangement required for vacancy annihilation, thereby enabling the retention of vacancy clusters and dislocation networks within the consolidated microstructure [31,32]. Figure 3(f) shows the selected area electron diffraction (SAED) pattern of $(Fe_{0.3}Mn_{0.7})_2AlB_2$. The observed diffraction spots corresponding to the $(\bar{2}00)$, $(01\bar{1})$, and $(0\bar{2}2)$ planes are in good agreement with the XRD data presented in Fig. 2(a). The inverse fast Fourier transform (IFFT)-filtered images (Figs. 3(g) and 3(h)) reveal the existence of lattice distortions. The emergence of these distortions is attributed to the difference in atomic radius between Mn and Fe, which can lead to local lattice expansion and consequent lattice distortions [33]. Additionally, Mn doping modifies the chemical bonding in Fe_2AlB_2, resulting in stronger coordination bonds between Mn and B. This change in coordination also contributes to the emergence of local lattice distortions. These lattice distortions promote the formation of

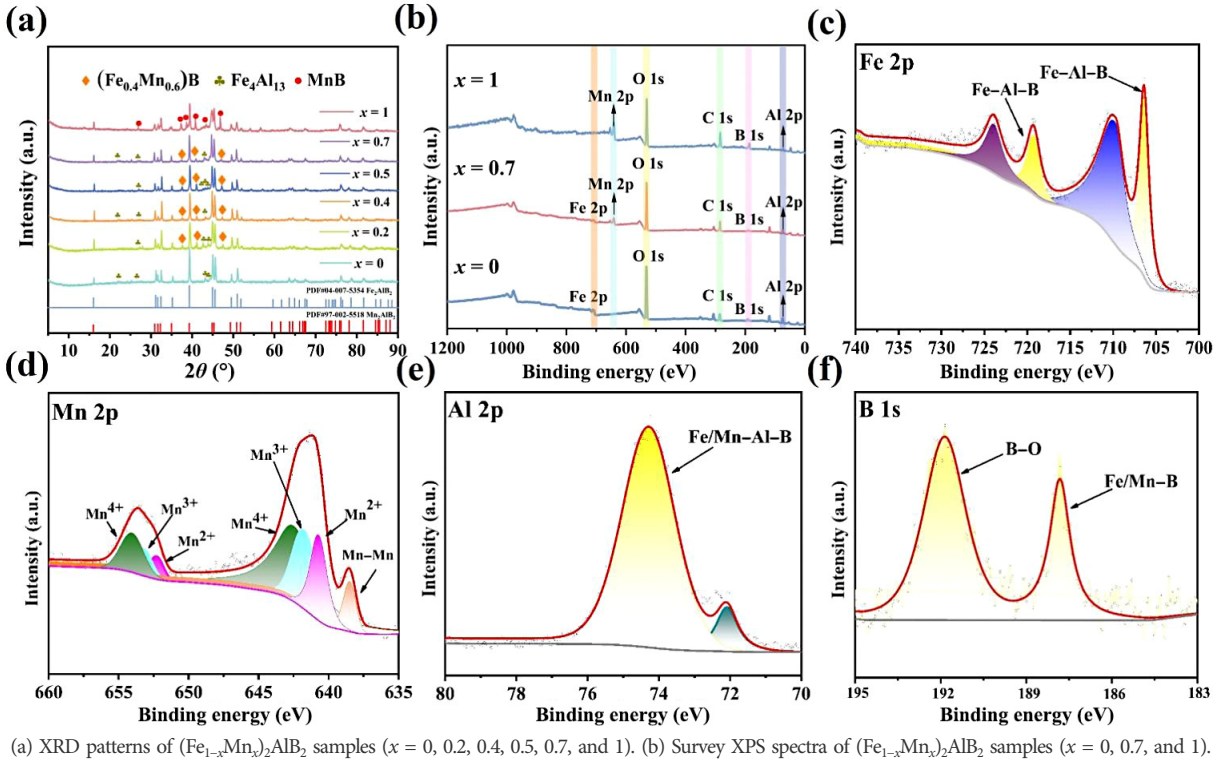

Fig. 2 (a) XRD patterns of $(Fe_{1-x}Mn_x)_2AlB_2$ samples (x = 0, 0.2, 0.4, 0.5, 0.7, and 1). (b) Survey XPS spectra of $(Fe_{1-x}Mn_x)_2AlB_2$ samples (x = 0, 0.7, and 1). High-resolution (c) Fe 2p, (d) Mn 2p, (e) Al 2p, and (f) B 1s XPS spectra of $(Fe_{0.3}Mn_{0.7})_2AlB_2$ sample.

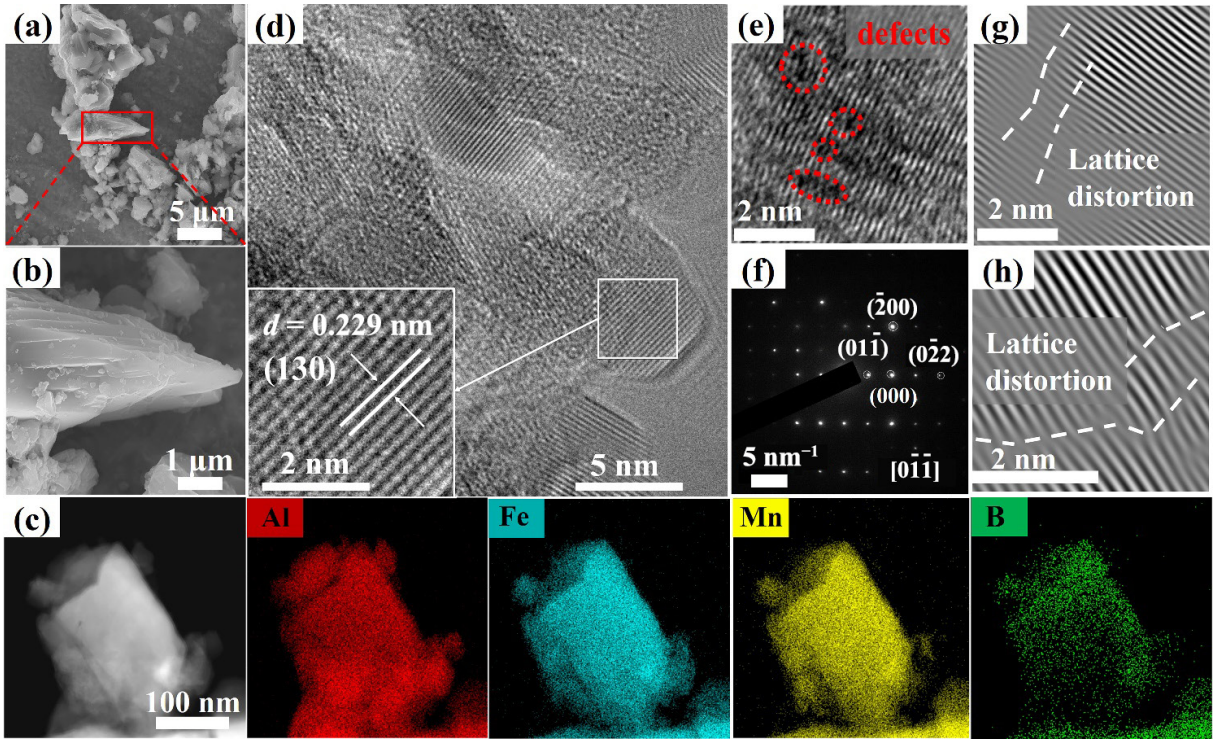

Fig. 3 (a, b) SEM images of $(Fe_{0.3}Mn_{0.7})_2AlB_2$. (c) HAADF-STEM image and corresponding Al, Mn, Fe, and B elemental mapping images of $(Fe_{0.3}Mn_{0.7})_2AlB_2$. (d, e) HRTEM image of $(Fe_{0.3}Mn_{0.7})_2AlB_2$ and (f) SAED pattern of $(Fe_{0.3}Mn_{0.7})_2AlB_2$ along $[0\bar{1}\bar{1}]$ zone axis. (g, h) Atomic IFFT-filtered images of $(Fe_{0.3}Mn_{0.7})_2AlB_2$ derived from SAED pattern.

defects [34]. As a result, defects and lattice distortions are generated within the material through a combination of Joule heating-driven ultrafast sintering and defect engineering. The presence of these defects and lattice distortions is expected to enhance the dielectric properties of the materials and improve their microwave absorption [35–41].

3.2 EMW absorption properties

The absorption characteristics of $(Fe_{1-x}Mn_x)_2AlB_2$ samples were evaluated by calculating their reflection loss (RL), which is a crucial parameter. RL is calculated as Eq. (1) and (2) [12]:

$$\mathrm{RL\ (dB)} = 20\log\left|\frac{Z_{in}-Z_0}{Z_{in}+Z_0}\right| \quad (1)$$

$$Z_{in} = Z_0\sqrt{\frac{u_r}{\varepsilon_r}}\tanh\left(\left(\frac{2\pi jfd}{c}\right)\sqrt{u_r\varepsilon_r}\right) \quad (2)$$

where Z_{in} is the impedance of the absorbing material; Z_0 is the characteristic impedance of the medium in which the wave propagates; f is the incoming microwave frequency; d is the thickness of the absorbing material; c is the speed of light.

In general, the RL value is employed to assess the absorbing performance of a material. The EMW absorption performance of $(Fe_{1-x}Mn_x)_2AlB_2$ samples (x = 0, 0.2, 0.4, 0.5, 0.7, and 1) was evaluated via VNA. Figures 4 and 5 depict the RL curves and two-dimensional (2D) RL contour maps of all samples with various thicknesses in the frequency range of 2–18 GHz. As illustrated in Figs. 4(a)–4(f), the $(Fe_{1-x}Mn_x)_2AlB_2$ samples with x = 0.2–0.7 exhibit excellent wave-absorption properties, with RL_{min} values of −34.23, −40.59, −43.8, and −47.8 dB, respectively, at a thickness of 1.5 mm. In contrast, the RL_{min} values of the samples with x = 0 and 1 are −25.72 and −14.21 dB, respectively, at thicknesses of 1.5 and 5 mm, respectively. Thus, the RL_{min} values of these samples initially increase with increasing x, reaches a peak of −47.8 dB at x = 0.7, and then decreases. As shown in Figs. 5(a)–5(f), EAB_{max} of the $(Fe_{1-x}Mn_x)_2AlB_2$ samples with x = 0.2–0.7 is significantly greater than that of the $(Fe_{1-x}Mn_x)_2AlB_2$ samples with x = 0 and 1. The maximum EAB_{max} (4.16 GHz) is reached at x = 0.7. These results indicate that the samples doped with Mn exhibit a greater EMW attenuation capacity than the undoped sample and the sample with Mn fully replacing Fe. Specifically, the sample with x = 0.7 possesses the strongest EMW attenuation capacity, and these outstanding wave-absorption characteristics will be discussed in detail later. These findings imply that introducing defects through doping is an effective strategy to enhance the EMW absorption capacity of materials. In addition, as shown in Fig. 5(g) and Table S3 in the ESM, $(Fe_{0.3}Mn_{0.7})_2AlB_2$ has better EMW absorption properties than most of the previously reported transition metal-layered compounds, confirming that $(Fe_{0.3}Mn_{0.7})_2AlB_2$ is promising as a highly efficient and lightweight EMW absorber for practical applications.

3.3 EMW absorption mechanism and EM parameters of $(Fe_{1-x}Mn_x)_2AlB_2$ samples

A comprehensive investigation of the dielectric constant ($\varepsilon_r = \varepsilon' - j\varepsilon''$) and magnetic permeability ($\mu_r = \mu - j\mu''$) in the 2–18 GHz frequency band is necessary to gain a deeper understanding of the microwave absorption mechanism of the $(Fe_{1-x}Mn_x)_2AlB_2$ samples. The EM energy storage capacity is represented by the real parts (ε' and μ'), whereas the ability to dissipate EM energy is represented by the imaginary parts (ε'' and μ''). Figure 6(a) illustrates that ε' exhibits a comparable fluctuating trend in the high-frequency range (10–18 GHz) for all samples, except for the undoped sample. This is attributed to the orientation of the polarization of the intrinsic electric dipoles and the polarization of the space charges in the high-frequency range (10–18 GHz) [42]. The undoped sample shows maxima in ε' at 6.9, 11.8, and

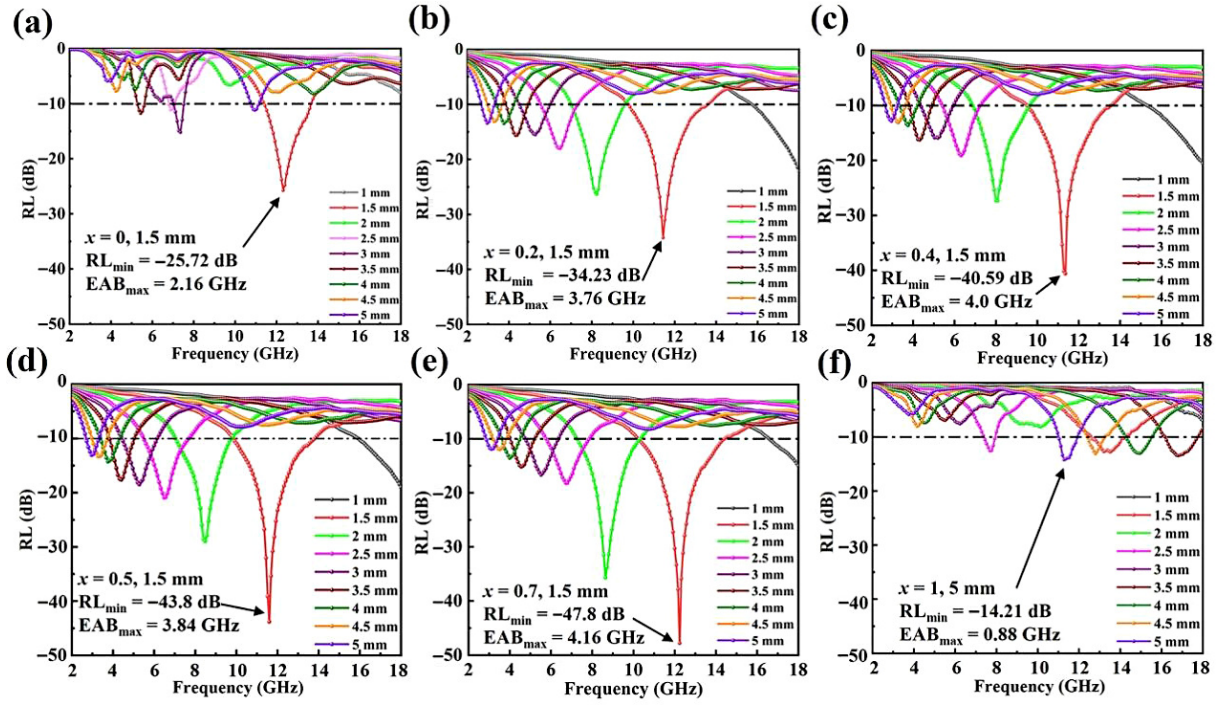

Fig. 4 RL curves of (a) Fe_2AlB_2, (b) $(Fe_{0.8}Mn_{0.2})_2AlB_2$, (c) $(Fe_{0.6}Mn_{0.4})_2AlB_2$, (d) $(Fe_{0.5}Mn_{0.5})_2AlB_2$, (e) $(Fe_{0.3}Mn_{0.7})_2AlB_2$, and (f) Mn_2AlB_2 with different thicknesses.

16.0 GHz and a decrease in ε' at higher frequencies. This can be attributed to the polarization lag that occurs under the influence of an electric field [27]. The multiple fluctuations observed for ε'' are attributed to dipole and interfacial polarizations (Fig. 6(b)). This polarization complexity originates from Mn-induced lattice distortions at M-sites coupled with defect generation during Joule-driven thermal cycling—a dual structural modification conclusively demonstrated through atomic IFFT-filtered and HRTEM images (Fig. 3). These defects and lattice distortions act as polarization centers, hindering the reorientation of dipoles and rearrangement of space charges under an alternating electric field. This results in energy dissipation, thereby increasing the dielectric loss of the material. The increase in dielectric loss is usually manifested as an increase in the imaginary part of the permittivity (ε'') [42]. The fluctuations in ε'' and dielectric loss tangent ($\tan\delta_\varepsilon = \varepsilon''/\varepsilon'$) illustrated in Figs. 6(b) and 6(c) are comparable for various samples, with multiple relaxation peaks within the 6–18 GHz range, indicating the possible occurrence of polarization relaxation phenomena [27].

The attenuation constant (α) is another important parameter for assessing the performance of EMW absorbers. It is calculated as Eq. (3) [43]:

$$\alpha = \left(\frac{\sqrt{2}\pi f}{c}\right) \times \sqrt{(u''\varepsilon'' - u'\varepsilon') + \sqrt{(u''\varepsilon'' - u'\varepsilon')^2 + (u''\varepsilon' + u'\varepsilon'')^2}} \quad (3)$$

The attenuation constant of the $(Fe_{1-x}Mn_x)_2AlB_2$ samples with x = 0.2–0.7 is typically greater than those of the $(Fe_{1-x}Mn_x)_2AlB_2$ samples with x = 0 and 1, with the highest attenuation constant observed at x = 0.7. This indicates that $(Fe_{0.3}Mn_{0.7})_2AlB_2$ exhibits exceptional EMW attenuation properties, as illustrated in Fig. 6(d). Additionally, this finding suggests that Mn incorporation at the M site of Fe_2AlB_2 is an effective method for enhancing its EMW attenuation capability.

Figure 6(e) illustrates that the overall μ' of the $(Fe_{1-x}Mn_x)_2AlB_2$ samples with x = 0.2–0.7 is reduced with increasing frequency. This can be attributed to the intrinsic magnetic resonance occurring in these samples. The μ values of the $(Fe_{1-x}Mn_x)_2AlB_2$ samples with x = 0 and 1 are lower than those of the other samples because the low saturation magnetization (M_S) of these two samples decreases their μ values (Fig. 7(a)) [44]. Furthermore, μ'' is usually used to evaluate the magnetic loss capability of a material. The μ'' of the $(Fe_{1-x}Mn_x)_2AlB_2$ samples initially increases with increasing x, reaches a maximum at x = 0.7 and subsequently decreases (Fig. 6(f)). This suggests that Mn doping enhances the magnetic loss capability of the $(Fe_{1-x}Mn_x)_2AlB_2$ samples. The magnetic loss tangent ($\tan\delta_\mu = \mu''/\mu'$) has a similar trend as a function of x as that of μ''. As illustrated in Fig. 6(g), the greatest magnetic loss tangent loss is observed at x = 0.7. Compared with the dielectric loss contribution, the magnetic loss contribution has a more pronounced effect on the overall EMW loss capacity of the $(Fe_{1-x}Mn_x)_2AlB_2$ samples. Magnetic losses mainly stem from domain wall resonance, hysteresis, eddy current loss, natural resonance, and exchange resonance. The domain wall resonance loss usually occurs at low frequencies (MHz) [45]. In addition, the eddy current loss can be estimated as Eq. (4) [46]:

$$C_0 = u''\left(u'\right)^{-2} f^{-1} = \frac{2\pi u_0 \sigma D^2}{3} \quad (4)$$

where σ represents the electrical conductivity of a material; D is the matching thickness; μ_0 denotes the vacuum permeability. Magnetic losses are caused only by eddy current losses if C_0 is a constant; otherwise, they are caused by exchange resonance or natural resonance [47]. As illustrated in Fig. 7(b), the curves of the C_0 values of the six samples as a function of frequency unambiguously demonstrate that magnetic resonance is the predominant source of magnetic loss in the $(Fe_{1-x}Mn_x)_2AlB_2$ samples. Concerning the magnetic resonance mechanism, the complex permeability spectra (μ''–f) of all samples can be fitted with the Landau–Lifshitz–Gilbert (LLG) equation [48], and the relationship is expressed as Eq. (5):

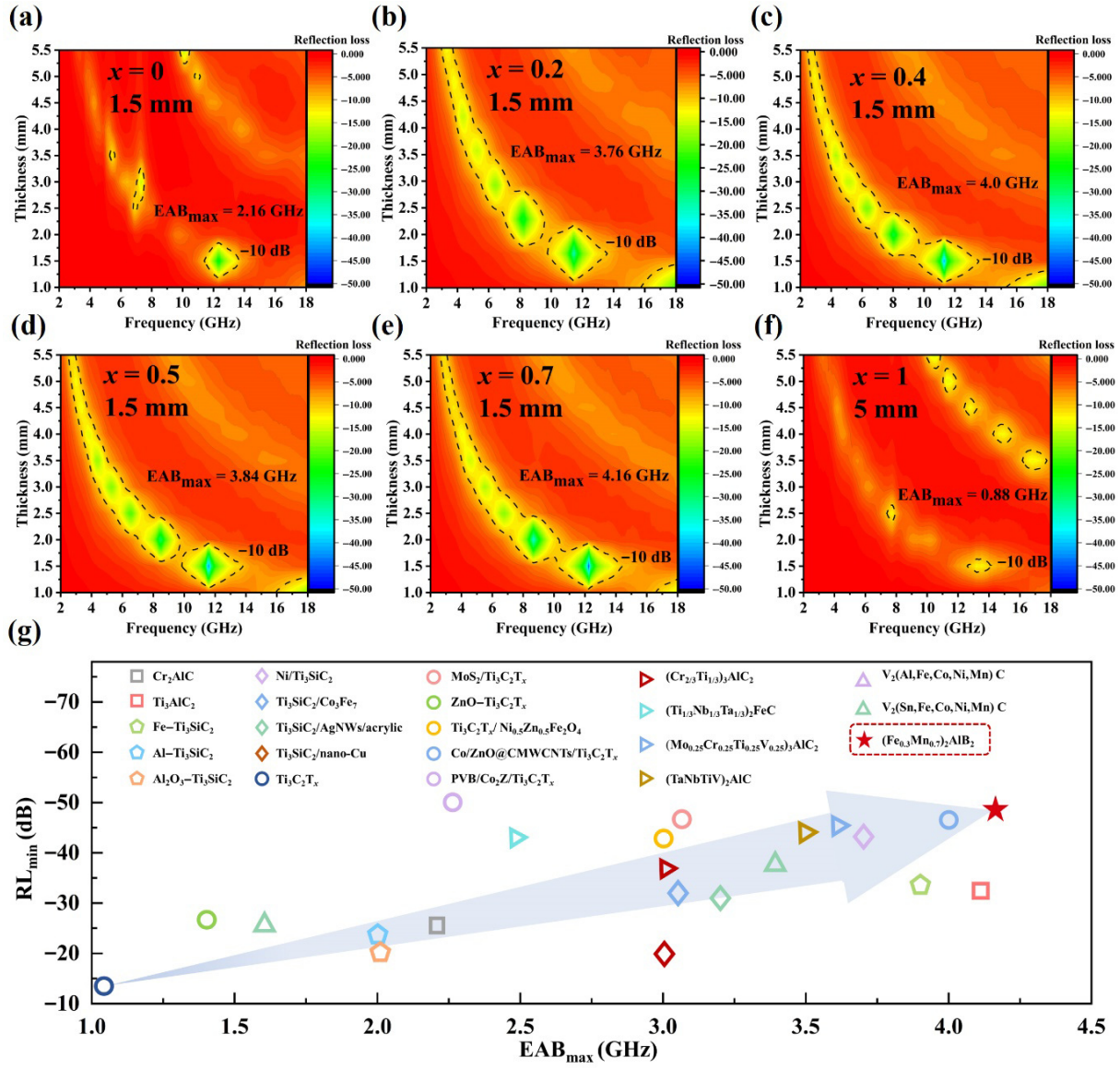

Fig. 5 2D RL contour maps of (a) Fe_2AlB_2, (b) $(Fe_{0.8}Mn_{0.2})_2AlB_2$, (c) $(Fe_{0.6}Mn_{0.4})_2AlB_2$, (d) $(Fe_{0.5}Mn_{0.5})_2AlB_2$, (e) $(Fe_{0.3}Mn_{0.7})_2AlB_2$, and (f) Mn_2AlB_2. (g) EMW absorption performance of $(Fe_{0.3}Mn_{0.7})_2AlB_2$ versus other transition metal-layered compound absorbers reported previously.

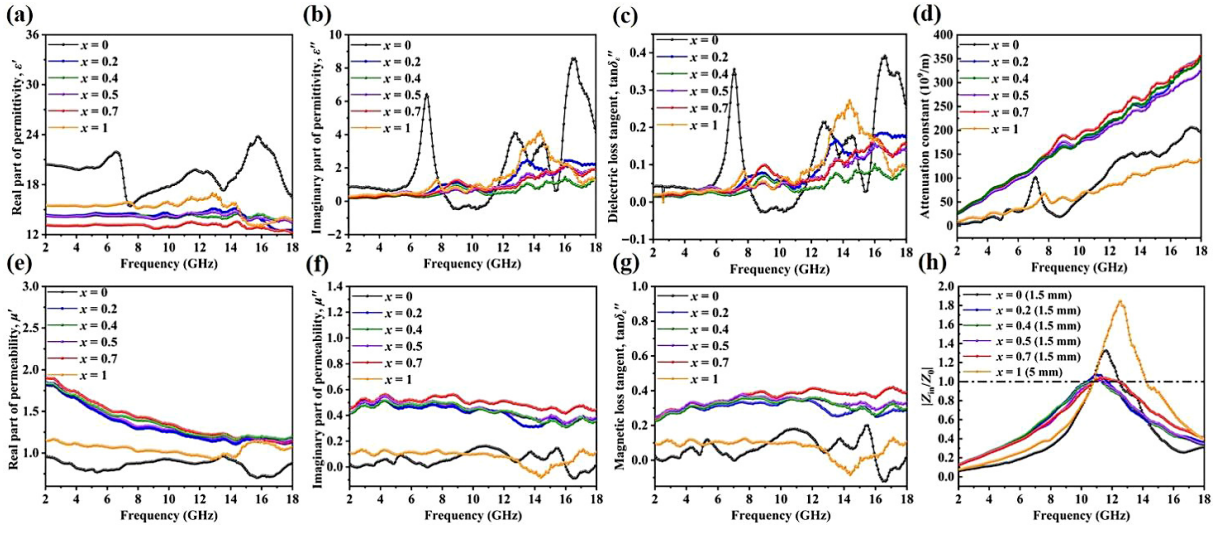

Fig. 6 EMW absorption properties of $(Fe_{1-x}Mn_x)_2AlB_2$ samples (x = 0, 0.2, 0.4, 0.5, 0.7, and 1): (a) real part of complex permittivity (ε'), (b) imaginary part of complex permittivity (ε''), (c) dielectric loss tangent ($\tan\delta_\varepsilon$), (d) attenuation constant (α), (e) real part of the complex permeability (μ'), (f) imaginary part of the complex permeability (μ''), (g) magnetic loss tangent ($\tan\delta_\mu$), and (h) Z_{in}/Z_0.

https://doi.org/10.26599/JAC.2025.9221057

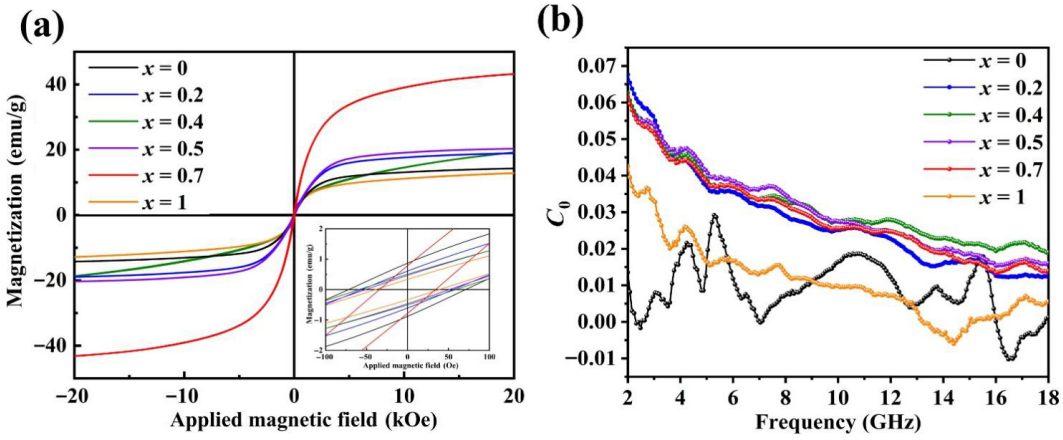

Fig. 7 (a) Hysteresis loops and (b) C_0 curves of the $(Fe_{1-x}Mn_x)_2AlB_2$ samples. The inset in panel (a) shows a magnified view of the loops in the magnetic field range from −100 to 100 Oe.

$$u'' = \sum_i^n x_i' \frac{\left(\frac{f}{f_i}\right)\beta\left[1+\left(\frac{f}{f_i}\right)^2\left(1+\beta^2\right)\right]}{\left[1-\left(\frac{f}{f_i}\right)^2\left(1+\beta^2\right)\right]^2+4\beta^2\left(\frac{f}{f_i}\right)^2} \quad (5)$$

where n is the number of μ'' peaks; x_i' is the initial magnetization; f_i is the natural resonance frequency; β is the damping factor. To understand the effect of hysteresis loss on the $(Fe_{1-x}Mn_x)_2AlB_2$ samples, their hysteresis return line was investigated, as shown in Fig. 7(a). The saturation magnetization and coercivity can be extracted from the hysteresis loops, and the corresponding values are provided in Table S4 in the ESM. As x increases, M_s also increases, reaching a maximum value of 43.2 emu/g at x = 0.7. Concurrently, the coercivity (H_c) declines and reaches a minimum value of 32.1 Oe at x = 0.7. The anomalous behavior of the sample with x = 0.7 can be attributed to the occurrence of a super-magnetic jump, as previously demonstrated by Shiotani *et al.* [14]. In this jump, the saturation magnetization of the material grows dramatically as the applied magnetic field increases [49]. This is due to the applied magnetic field disrupting the initial antiferromagnetic order, leading to a progressive tendency of the magnetic moments to align parallel to each other and a consequent increase in the saturation magnetization of the material. $(Fe_{0.3}Mn_{0.7})_2AlB_2$ is readily magnetized and exhibits a rapid response to external electromagnetic fields owing to its high saturation magnetization and low coercivity. This increases the energy consumption during the rotation of the magnetic domains [42]. In conclusion, magnetic resonance and hysteresis loss are the two primary magnetic loss mechanisms in the investigated samples. Both processes are capable of efficiently dissipating EM energy. In addition, optimized impedance matching ($Z = |Z_{in}/Z_0|$) results in high EMW absorption performance [50,51]. A Z value of 1 indicates that the impedance matching of the material is optimal, which facilitates the penetration of EMW into the material and its effective absorption [52]. As shown in Fig. 6(h), for the $(Fe_{1-x}Mn_x)_2AlB_2$ samples with x = 0.2–0.7, the thickness at which RL is minimum corresponds to a Z value close to 1. The $(Fe_{1-x}Mn_x)_2AlB_2$ samples exhibit improved impedance matching, demonstrating that Mn doping plays a key role in modulating the impedance matching properties of Fe_2AlB_2. Specifically, over a broader frequency range, the Z value of $(Fe_{0.3}Mn_{0.7})_2AlB_2$ approaches 1. This indicates that the excellent impedance matching of $(Fe_{0.3}Mn_{0.7})_2AlB_2$ contributes to the outstanding EMW absorption performance of this sample.

The dipole polarization relaxation can be explained by the Debye relaxation theory, and the relationship between ε' and ε'' can be expressed as Eq. (6)[53]:

$$\left(\varepsilon' - \frac{\varepsilon_s+\varepsilon_\infty}{2}\right)^2 + (\varepsilon'')^2 = \left(\frac{\varepsilon_s-\varepsilon_\infty}{2}\right)^2 \quad (6)$$

where ε_∞ and ε_s represent the dielectric constant at infinite frequency and the static dielectric constant, respectively. If ε' and ε'' satisfy the condition set out in Eq. (6), the ε''–ε' curve will form a semicircle, which is known as the Cole–Cole semicircle. This behavior, as illustrated in Figs. 8(a) and 8(f), occurs when the polarization loss is solely due to dipole polarization relaxation. Each semicircle corresponds to a Debye dipole relaxation process. As mentioned above, polarization relaxation loss leads to dielectric loss, which manifests itself with fluctuations in the tanδ_ε curve (Fig. 6(c)) in the frequency range of 2–18 GHz as well as the Cole–Cole diagrams in Fig. 8. As depicted in Fig. 8, the ε''–ε' curves demonstrate multiple distinct Cole–Cole semicircles, where an increased semicircle multiplicity correlates with enhanced polarization relaxation processes within the absorber. In Figs. 8(a) and 8(f), the limited semicircle multiplicity reflects restricted polarization mechanisms, which can be attributed to constrained polarization mechanisms. In contrast, Figs. 8(b)–8(e) display multiple distorted and non-standard semicircles, indicative of simultaneous activation of dipole polarization and interfacial polarization under alternating electromagnetic fields [45]. This phenomenon primarily stems from doping-induced structural modifications. Mn/Fe substitution significantly increases heterogeneous interfaces, thereby amplifying the interfacial polarization. When irradiated by EMW, interfacial charge accumulation occurs at both stacked interlayer boundaries and phase interfaces (e.g., between $(Fe_{1-x}Mn_x)_2AlB_2$ matrix and secondary phases), inducing interfacial polarization relaxation [13]. Concurrently, the doping process introduces lattice distortion defects and vacancy clusters, which function as dipole polarization centers. These defect-induced dipoles exhibit enhanced oscillation synchronization with incident EMW, substantially improving the dipole polarization efficiency.

The mechanisms of EMW absorption are illustrated in Fig. 9, taking the $(Fe_{0.3}Mn_{0.7})_2AlB_2$ sample as an example. As a conventional MAB phase, $(Fe_{0.3}Mn_{0.7})_2AlB_2$ has good electrical conductivity because of the strong metallic bonding within the M layer. Consequently, it can provide conduction losses by generating heat and dissipating EMW. Furthermore, Mn is incorporated at the M site of $(Fe_{0.3}Mn_{0.7})_2AlB_2$, where it replaces Fe, resulting in an uneven charge distribution. This uneven charge

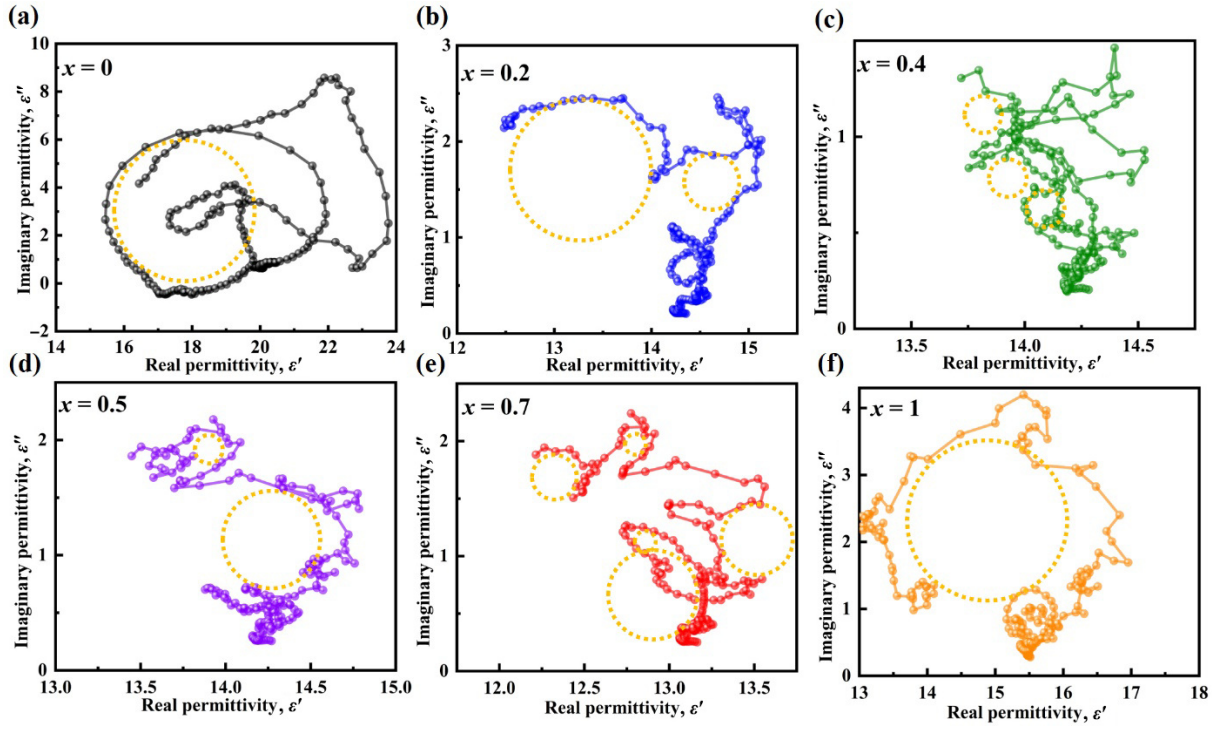

Fig. 8 Cole–Cole diagrams of $(Fe_{1-x}Mn_x)_2AlB_2$ samples with (a) $x = 0$, (b) $x = 0.2$, (c) $x = 0.4$, (d) $x = 0.5$, (e) $x = 0.7$, and (f) $x = 1$.

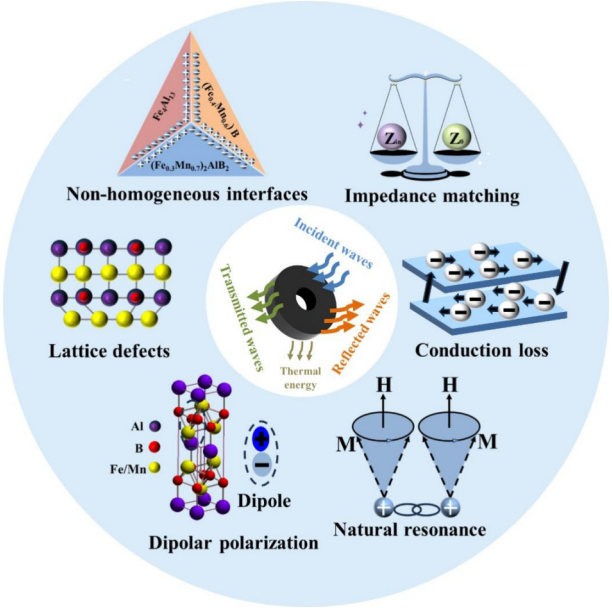

Fig. 9 Microwave absorption mechanisms of $(Fe_{0.3}Mn_{0.7})_2AlB_2$.

distribution leads to dipole enrichment and promotes the relaxation process of dipole polarization. In addition, non-homogeneous interfaces with different charge distributions form between $(Fe_{0.3}Mn_{0.7})_2AlB_2$ and various constituent phases, namely, Fe_4Al_{13} and $(Fe_{0.4}Mn_{0.6})B$. These interfaces give rise to multiple interfacial polarization relaxation processes, thereby increasing EMW attenuation. Doping with Mn, combined with rapid sintering and cooling processes, leads to the formation of defects and lattice distortions. Consequently, the free electrons in $(Fe_{0.3}Mn_{0.7})_2AlB_2$, when subjected to an external electric field, accumulate at these defects and lattice distortions, resulting in space charge polarization. Finally, magnetic resonance loss and hysteresis loss are the dominant contributors to the magnetic loss of $(Fe_{0.3}Mn_{0.7})_2AlB_2$. $(Fe_{0.3}Mn_{0.7})_2AlB_2$ exhibits high saturation magnetization and low coercivity, which results in a rapid response to external EM fields and increased energy dissipation during the rotation of the magnetic domains. Therefore, Mn doping combined with Joule heating-driven ultrafast synthesis not only enhances conduction loss, polarization loss, magnetic resonance loss, and hysteresis loss but also promotes the formation of defects. As a result of these synergistic effects, both the dielectric and magnetic losses of the $(Fe_{1-x}Mn_x)_2AlB_2$ samples are increased, leading to outstanding EMW absorption performance.

4 Conclusions

In conclusion, we successfully synthesized $(Fe_{1-x}Mn_x)_2AlB_2$ samples ($x = 0$, 0.2, 0.4, 0.5, 0.7, and 1) using Joule heating-driven ultrafast synthesis, resulting in improved EMW absorption performance. Mn doping enhances dielectric loss through defects and lattice distortions, leading to stronger EMW attenuation for samples with $x = 0.2$–0.7. Notably, owing to the occurrence of a super-magnetic jump in $(Fe_{0.3}Mn_{0.7})_2AlB_2$, the saturation magnetization and magnetic loss of the material are enhanced. As a result, $(Fe_{0.3}Mn_{0.7})_2AlB_2$ exhibits exceptional EMW absorption, with EAB_{max} of 4.16 GHz and RL_{min} of −47.8 dB at an ultralow thickness of 1.5 mm. This work demonstrates an innovative approach for synthesizing MAB phases and establishes a defect engineering framework to enhance their EMW absorption performance. Future studies should harness this integrated methodology to explore advanced MAB phases while precisely tuning defect configurations. These synergistic efforts could propel the development of MAB materials with programmable electromagnetic functionalities for emerging applications.

Acknowledgements

We thank eceshi (www.eceshi.com) for the XRD and XPS analysis.

Author contributions

Yuhang Bai: Methodology, investigation, data curation, and writing - review & editing. Zelong Yao: Investigation, formal analysis, and writing - original draft. Yang Yang: Data curation and investigation. Jinrui Li: Investigation. Jia Liu: Methodology. Peipei Wang: Methodology. Huiling Du: Project administration. Xing Zhao: Formal analysis, project administration, and supervision. Laifei Cheng: Funding acquisition, project administration, resources, and writing - review & editing.

Availability of data and materials

The data that support the findings of this study are available from the corresponding author upon reasonable request.

Competing interests

The authors have no competing interests to declare that are relevant to the content of this article.

Electronic Supplementary Material

Supplementary material is available in the online version of this article at https://doi.org/10.26599/JAC.2025.9221057.

Funding

This work was financially supported by the National Natural Science Foundation of China (Nos. 52202069, 52402089, and 52102144) and the Young Talent Fund of the Xi'an Association for Science and Technology (No. 959202313074).

References

[1] Cao Q, Zhang J, Zhang HB, *et al.* Dual-surfactant templated hydrothermal synthesis of $CoSe_2$ hierarchical microclews for dielectric microwave absorption. *J Adv Ceram* 2022, **11**: 504–514.

[2] Hu FY, Zhang F, Wang XH, *et al.* Ultrabroad band microwave absorption from hierarchical $MoO_3/TiO_2/Mo_2TiC_2T_x$ hybrids via annealing treatment. *J Adv Ceram* 2022, **11**: 1466–1478.

[3] Niu HH, Jiang XW, Xia YD, *et al.* Construction of *hydrangea*-like core–shell $SiO_2@Ti_3C_2T_x$@CoNi microspheres for tunable electromagnetic wave absorbers. *J Adv Ceram* 2023, **12**: 711–723.

[4] Wang SP, Liu QC, Li SK, *et al.* Joule-heating-driven synthesis of a honeycomb-like porous carbon nanofiber/high entropy alloy composite as an ultralightweight electromagnetic wave absorber. *ACS Nano* 2024, **18**: 5040–5050.

[5] Wang ZJ, Zhang F, Wang NN, *et al.* Ternary layered boride MoAlB: A novel thermo-regulation microwave absorbing ceramic material. *J Adv Ceram* 2024, **13**: 699–710.

[6] Wu CW, Zhang F, Zhi Q, *et al.* From binary to ternary and back to binary: Transition of electromagnetic wave shielding to absorption among MAB phase Ni_3ZnB_2 and corresponding binary borides $Ni_{n+1}B_n$ (n = 1, 3). *J Adv Ceram* 2023, **12**: 2101–2111.

[7] Kota S, Sokol M, Barsoum MW. A progress report on the MAB phases: Atomically laminated, ternary transition metal borides. *Int Mater Rev* 2020, **65**: 226–255.

[8] Li N, Bai YL, Wang S, *et al.* Rapid synthesis, electrical, and mechanical properties of polycrystalline Fe_2AlB_2 bulk from elemental powders. *J Am Ceram Soc* 2017, **100**: 4407–4411.

[9] Cedervall J, Andersson MS, Sarkar T, *et al.* Magnetic structure of the magnetocaloric compound $AlFe_2B_2$. *J Alloys Compd* 2016, **664**: 784–791.

[10] Levin EM, Jensen BA, Barua R, *et al.* Effects of Al content and annealing on the phases formation, lattice parameters, and magnetization of $Al_xFe_2B_2$ (x = 1.0, 1.1, 1.2) alloys. *Phys Rev Mater* 2018, **2**: 034403.

[11] Luo W, Liu Y, Wang CY, *et al.* Molten salt assisted synthesis and electromagnetic wave absorption properties of $(V_{1-x-y}Ti_xCr_y)_2AlC$ solid solutions. *J Mater Chem C* 2021, **9**: 7697–7705.

[12] Li J, Xu TT, Bai H, *et al.* Structural modifications and electromagnetic property regulations of Ti_3AlC_2 MAX for enhancing microwave absorption through the strategy of Fe doping. *Adv Mater Interfaces* 2022, **9**: 2101510.

[13] Han JX, Chen QY, Wang YZ, *et al.* Anomalous electromagnetic wave absorption of MAX phase ceramic powder achieved through high entropy solid solution and melt pool heat transfer preparation method. *J Mater Sci—Mater El* 2024, **35**: 883.

[14] Shiotani T, Waki T, Tabata Y, *et al.* Competing magnetic correlations and uniaxial anisotropy in $(Fe_{1-x}Mn_x)_2AlB_2$ single crystals. *Phys Rev Mater* 2024, **8**: 054412.

[15] Melikhov Y, Snyder JE, Jiles DC, *et al.* Temperature dependence of magnetic anisotropy in Mn-substituted cobalt ferrite. *J Appl Phys* 2006, **99**: 08R102.

[16] Jia JG, Liu CY, Ma N, *et al.* Exchange coupling controlled ferrite with dual magnetic resonance and broad frequency bandwidth in microwave absorption. *Sci Technol Adv Mat* 2013, **14**: 045002.

[17] Wang CW, Ping WW, Bai Q, *et al.* A general method to synthesize and sinter bulk ceramics in seconds. *Science* 2020, **368**: 521–526.

[18] Ramasamy S. Investigation of nanostructured materials by positron annihilation. *Met Mater Process* 1996, **8**: 61–73.

[19] Kusunoki H, Kondo T, Hiraki K, *et al.* Grain-size dependence of absorption characteristics of the electromagnetic wave absorbers of ferrite–SiO_2 composites. *Electr Eng Jpn* 2004, **146**: 1–9.

[20] Bowen CR, Open J, Fitzmaurice J, *et al.* Fast firing of electroceramics. *Ferroelectrics* 1999, **228**: 159–166.

[21] Biesuz M, Spiridigliozzi L, Frasnelli M, *et al.* Rapid densification of samarium-doped Ceria ceramic with nanometric grain size at 900–1100 °C. *Mater Lett* 2017, **190**: 17–19.

[22] Esposito V, Traversa E. Design of electroceramics for solid oxides fuel cell applications: Playing with ceria. *J Am Ceram Soc* 2008, **91**: 1037–1051.

[23] Bai YH, Li JR, Lu H, *et al.* Ultrafast high-temperature sintering of high-entropy oxides with refined microstructure and superior lithium-ion storage performance. *J Adv Ceram* 2023, **12**: 1857–1871.

[24] Zhao X, Wu WT, Bai YH, *et al.* Microstructure evolution and densification behavior of ultrafast high-temperature sintered $Li_{6.5}La_3Zr_{1.5}Ta_{0.5}O_{12}$ ceramics. *J Power Sources* 2024, **613**: 234913.

[25] Liu J, Li SB, Yao BX, *et al.* Rapid synthesis and characterization of a nanolaminated Fe_2AlB_2 compound. *J Alloys Compd* 2018, **766**: 488–497.

[26] Liang BY, Zhu DD, Zhang Q, *et al.* Preparation of Mn_2AlB_2 material via thermal explosion. *Russ J Non-Ferr Met* 2022, **63**: 448–455.

[27] Zhi Q, Wu CW, Li MR, *et al.* Fe_2AlB_2: A novel ferromagnetic material with superior electromagnetic wave absorption performance. *Ceram Int* 2023, **49**: 34182–34190.

[28] Benamor A, Hadji Y, Kota S, *et al.* Friction and wear characteristics of the nanolaminated ternary transition metal boride: Mn_2AlB_2. *Wear* 2022, **492–493**: 204232.

[29] Natu V, Kota SS, Barsoum MW. X-ray photoelectron spectroscopy of the MAB phases, MoAlB, M_2AlB_2 (M = Cr, Fe), Cr_3AlB_4 and their binary monoborides. *J Eur Ceram Soc* 2020, **40**: 305–314.

[30] Potanin AY, Bashkirov EA, Karpenkov AY, *et al.* Fabrication of high-strength magnetocaloric Fe_2AlB_2 MAB phase ceramics via combustion synthesis and hot pressing. *Materialia* 2024, **33**: 101993.

[31] Mishra TP, Wang SF, Lenser C, *et al.* Ultra-fast high-temperature sintering of strontium titanate. *Acta Mater* 2022, **231**: 117918.

[32] German RM. Rapid heating concepts in sintering. *J Powder Mater* 2013, **20**: 85–99. (in Korean)

[33] Lesturgez S, Goglio G, Duttine M, *et al.* Tuning the Mn and Fe valence states into new $Ca_{0.7}Mn_{2-x}Fe_xO_4$ ($0 < x \leq 0.60$) solid solution during reversible redox processes. *Chem Mater* 2016, **28**: 4935–4944.

[34] Qiu ZR, Liu XY, Yang TY, *et al.* Synergistic enhancement of electromagnetic wave absorption and corrosion resistance properties of high entropy alloy through lattice distortion engineering. *Adv Funct Mater* 2024, **34**: 2400220.

[35] Meng BS, Klein BDB, Booske JH, *et al.* Microwave absorption in

insulating dielectric ionic crystals including the role of point defects. *Phys Rev B* 1996, **53**: 12777–12785.
[36] Guo WJ, Ma ZY, Luo Y, *et al.* Structure, defects, and microwave dielectric properties of Al-doped and Al/Nd co-doped $Ba_4Nd_{9.33}Ti_{18}O_{54}$ ceramics. *J Adv Ceram* 2022, **11**: 629–640.
[37] Wang F, Gu WH, Chen JB, *et al.* The point defect and electronic structure of K doped $LaCo_{0.9}Fe_{0.1}O_3$ perovskite with enhanced microwave absorbing ability. *Nano Res* 2022, **15**: 3720–3728.
[38] Zhang WM, Xiang HM, Dai FZ, *et al.* Achieving ultra-broadband electromagnetic wave absorption in high-entropy transition metal carbides (HE TMCs). *J Adv Ceram* 2022, **11**: 545–555.
[39] Zhang WM, Zhao B, Xiang HM, *et al.* One-step synthesis and electromagnetic absorption properties of high entropy rare earth hexaborides (HE REB_6) and high entropy rare earth hexaborides/borates (HE REB_6/HE $REBO_3$) composite powders. *J Adv Ceram* 2021, **10**: 62–77.
[40] Xiang HM, Xing Y, Dai FZ, *et al.* High-entropy ceramics: Present status, challenges, and a look forward. *J Adv Ceram* 2021, **10**: 385–441.
[41] Ma JB, Zhao B, Xiang HM, *et al.* High-entropy spinel ferrites MFe_2O_4 (M = Mg, Mn, Fe, Co, Ni, Cu, Zn) with tunable electromagnetic properties and strong microwave absorption. *J Adv Ceram* 2022, **11**: 754–768.
[42] Liu XY, Tian FY, Sheng J, *et al.* High-entropy porous spinel ferrite @ amorphous carbon nanocomposites with abundant structural defects for wide-band electromagnetic wave absorption. *Chem Eng J* 2024, **490**: 151848.
[43] Xu XQ, Li DS, Li L, *et al.* Architectural design and microstructural engineering of metal-organic framework-derived nanomaterials for electromagnetic wave absorption. *Small Struct* 2023, **4**: 2200219.
[44] Tian F, Gao Y, Wang AP, *et al.* Effect of Mn substitution on structural, magnetic and microwave absorption properties of Co_2Y hexagonal ferrite. *J Magn Magn Mater* 2023, **587**: 171229.
[45] Liu YJ, Li HF, Yan XT, *et al.* Ultra-broadband microwave absorption of $(Mn_{0.2}Fe_{0.2}Zn_{1.2})_x$ substituted Co_2Y hexaferrites with a self-aligned sheet stacked, highly *c*-axis oriented and multi-domain structure. *J Mater Chem A* 2023, **11**: 26285–26300.
[46] Ghosh K, Srivastava SK. Fabrication of N-doped reduced graphite oxide/$MnCo_2O_4$ nanocomposites for enhanced microwave absorption performance. *Langmuir* 2021, **37**: 2213–2226.
[47] Luo X, Li HF, Deng DD, *et al.* Preparation and excellent electromagnetic absorption properties of dendritic structured Fe_3O_4@PANI composites. *J Alloys Compd* 2022, **891**: 161922.
[48] Wang XY, Wei SC, Wang B, *et al.* Doping sites, magnetic, and microwave absorption properties of barium ferrites with multiple magnetic resonances. *J Mater Sci—Mater El* 2023, **34**: 310.
[49] Kitagawa R, Kohashi T, Tsuji T, *et al.* Wide-field imaging of the magnetization process in soft magnetic-thin film using diamond quantum sensors. *Appl Phys Express* 2024, **17**: 017002.
[50] Song LM, Wu CW, Zhi Q, *et al.* Multifunctional SiC aerogel reinforced with nanofibers and nanowires for high-efficiency electromagnetic wave absorption. *Chem Eng J* 2023, **467**: 143518.
[51] Yang JC, Wen QB, Feng B, *et al.* Microstructural evolution and electromagnetic wave absorbing performance of single-source-precursor-synthesized SiCuCN-based ceramic nanocomposites. *J Adv Ceram* 2023, **12**: 1299–1316.
[52] Jiang XW, Niu HH, Li JL, *et al.* Construction of core-shell structured SiO_2@MoS_2 nanospheres for broadband electromagnetic wave absorption. *Appl Surf Sci* 2023, **628**: 157355.
[53] Quan B, Liang XH, Ji GB, *et al.* Dielectric polarization in electromagnetic wave absorption: Review and perspective. *J Alloys Compd* 2017, **728**: 1065–1075.